Fusing damage-sensitive features and domain adaptation towards robust damage classification in real buildings

Panagiotis Martakis [a,*], Yves Reuland [a], Andreas Stavridis [b], Eleni Chatzi [a]

[a] *Chair of Structural Mechanics and Monitoring, Department of Civil, Environmental, and Geomatic Engineering, ETH Zurich, Switzerland*
[b] *Structural Engineering and Earthquake Simulation Laboratory, Department of Civil, Structural, and Environmental Engineering, University at Buffalo, Buffalo, NY, USA*

ARTICLE INFO

ABSTRACT

Structural Health Monitoring (SHM) enables the rapid assessment of structural integrity in the immediate aftermath of strong ground motions. Data-driven techniques, often relying on damage-sensitive features (DSFs) derived from vibration monitoring, may be deployed to attribute a specific damage class to a structure. In practical applications, individual features are sensitive to specific levels of damage, and therefore combining multiple DSFs is required to formulate robust damage indicators. However, the combination of DSFs typically involves empirical thresholds that are often structure-specific and hinder generalization to different structural configurations. This work evaluates the predictive performance of a large ensemble of DSFs, computed on an extensive dataset of nonlinear simulations of frame structures with varying geometrical and material configurations. Gradient-boosted decision trees and convolutional neural networks are deployed to fuse multiple DSFs into damage classifiers, improving the predictive accuracy compared to best-practice methods and individual DSFs. A Domain Adversarial Neural Network (DANN) architecture enables the transfer of knowledge obtained from numerical simulations to real data from a large-scale shake-table test. After exposure to limited data, exclusively from the healthy state, the DANN framework yields satisfactory performance in predicting unseen damage states in the experimental dataset. The results demonstrate the potential of DANN in transferring knowledge from simulations to real-world monitoring applications, where only limited data characterizing exclusively the current, typically healthy, structural state is available. Overall, this work comprises the definition of multiple DSFs, their fusion through ML approaches, and the generalization of the knowledge obtained from simulations to real data through domain adaptation.

1. Introduction

Although modern seismic design codes have reduced the risk of casualties from earthquake events, performance-based design approaches tolerate structural damage, which is somehow against the principle of resilience. A main associated drawback is the required functional downtime of structures, which is incurred by lengthy and potentially subjective post-earthquake inspections [1,2]. Permanently monitored buildings can be leveraged for rapid and data-informed assessment of the post-earthquake structural integrity. Although extended literature has addressed data-driven damage detection in the past, the mere detection of the presence of damage after an earthquake is often insufficient for decision-makers. The quantification of damage sustained by an earthquake, often lumped into categorical damage states (DSs) [3,4], is further required for a reliable decision, as this offers insights into the

increase in vulnerability due to the main shock [5], paving the way to the critically important evaluation of residual capacity [6].

Structural Health Monitoring (SHM) often relies on changes in vibration properties to extract indicators of damage [7,8]. Changes in natural frequencies and, less frequently, damping coefficients are typically linked to the existence of damage [9–15], while modal shapes or mode-shape curvature may correlate with its location [16–19]. As data often proves insufficient, physics-based models are sometimes used to further improve performance in terms of damage detection and localization [20–24]. The aforementioned tasks comprise only the first two levels of damage identification [25], and do not typically entail a quantification of damage (third level), which may then lead to remaining useful life assessment (fourth level). In achieving these higher-end tasks, model-based SHM is typically exploited but involves the use of computationally expensive and structure-specific models [26–28].

In recent years, the increasingly available computational resources have entailed a paradigm shift from traditional vibration monitoring to the use of machine learning (ML) and deep learning applications [29]. ML algorithms provide powerful tools for training classifiers to differentiate healthy from damaged monitoring data or even attribute data to various classes related to increasing severity of damage [30–34]. In the context of post-earthquake assessment, Yuan et al. [35] trained a convolutional neural network (NN) for post-earthquake damage prediction, reaching an accuracy of 80% in model predictions. However, generalizing predictions from ML algorithms, trained on simulated data, to real structures is not trivial, while such references are very limited in the current literature. Tsuchimoto et al. [36] successfully predicted post-earthquake DSs in a scaled high-rise building, based on the residuals between the measured and modeled accelerations. Sajedi and Liang [37] trained support-vector machines on a large set of simulations to build a damage severity classifier, yielding a prediction accuracy of over 90% in a large-scale test specimen. Labeled data from real earthquake-damaged structures is scarce, and thus real-world monitoring datasets are often unbalanced or even limited to healthy data. Hence, supervised ML approaches that require large amount of labeled data cannot be directly applied. Recently, the combination of a limited number of buildings for damage assessment at larger scales has been proposed as an alternative to overcome the lack of historic labeled data [38–40].

Given the scarcity of real-world data from damaged structures, researchers rely on simulations to generate data in damaged states [41–43]. However, engineering models contain inherent bias and multiple sources of uncertainty that prevent a realistic representation of measured responses. A remedy to this can be sought in transfer learning; a ML technique, which aims to transfer knowledge from a source domain, where a large amount of labeled data is available, to a target domain with limited data [44]. Domain adaptation addresses this task by reducing the distance between the data distributions of the source and the target domains. Gardner et al. [41] outlined three domain adaptation methods, namely Transfer Component Analysis, Joint Domain Adaption, and Adaptation Regularization based Transfer Learning. Their applicability for vibration-based SHM is shown in various numerical cases and one hybrid case study, where the source domain comprises simulated data and the target domain contains measurements of a small-scale laboratory experiment. Bull et al. [45] proposed population-based SHM based on transfer component analysis to match the normal condition data from different wind-turbines, which leads to a 87% increase in the true positive rate. Ganin and Lempitsky [46] introduced a novel measure of the disparity between the source and target distributions by implementing a unified architecture that combines feature extraction, damage classification, and domain adaptation. This generic architecture, termed Domain Adversarial Neural Network (DANN), has been implemented for fault diagnosis in industrial machinery, demonstrating satisfactory performance and a reduced training time [47]. Ozdagli and Koutsoukos [48] deployed a DANN architecture to a benchmark dataset of vibration data corresponding to various DSs of a generic gearbox system. By differentiating the data into source and target domains, depending on the excitation amplitude, they demonstrated that the predictive performance of the adopted DANN architecture in the target domain outperforms source-only trained models, as well as other domain adaptation techniques. The authors used two source domains comprising the acceleration response of a low- and a high-fidelity numerical model, while the target domain contains the vibration recordings from a small-scale shake-table experiment. They demonstrated the inability of DANN to improve the predictive performance in the target response when the low-fidelity model is used as the source domain. For the high-fidelity model, the performance of the DANN architecture is consistently higher than that of the model trained only in the source domain. Xu and Noh [43] introduced a variation of the DANN architecture that considers weight factors in the loss function, depending on the similarity between the source data and the target domain. Simulations of a generic steel-frame structure with varying number of floors comprise the source domain, while the target domain consists of a small-scale four-story steel frame tested on a shake-table. The researchers formulated a similarity function that compares the number of floors between the source data and the experimental structure. The results demonstrate 70% accuracy in damage quantification in the target domain and improved performance, compared to the conventional DANN architecture. Although physics-based information is shown to be useful in the weighting of the source data, defining a similarity relation is not straightforward in real-world cases, where the source data differ from the target in more dimensions than only the number of floors (e.g., stiffness and mass distribution per floor, material properties, boundary conditions). This limitation becomes particularly relevant in cases, where the target domain includes large-scale structures consisting of inhomogeneous materials, such as concrete or masonry, with significant uncertainties in terms of material properties and boundary conditions.

Engineering demand parameters (EDPs), often structural displacements or drifts, are used in performance-based earthquake engineering [49,50] to define thresholds that separate DSs. For regional risk assessment, global EDPs, such as average roof drift (ARD), enable the derivation of fragility functions that link the probability of reaching a given DS with intensity measures that characterize the ground motion [51,52]. Similarly, monitoring-based damage quantification in buildings may involve a model-based derivation of fragility functions with respect to individual measurable DSFs, such as changes in natural frequencies [53] or modal features derived with wavelet decomposition [54]. Yet, formal comparison of the predictive performance of individual damage metrics on the basis of an extensive dataset of different building configurations is lacking. The applications of ML approaches to fuse DSFs are limited, while no domain adaptation applications to generalize predictions in real-world large-scale structures with inhomogeneous materials, such as concrete or masonry, have been attempted.

This paper capitalizes on novel ML tools and DSFs extracted from vibration-based (i.e., acceleration) response in simulations, in order to enhance damage quantification in real building structures. In Section 2 the methodological framework is presented, covering the creation of a parametric nonlinear model simulator, the formulation of a comprehensive ensemble of DSFs, and the architectures of the deployed ML and domain adaptation algorithms. Then, the classification performance of individual DSFs is compared with fragility curves, typically based on ground motion intensity, before the performance of classifiers that fuse several DSFs is assessed (Section 3). Finally, a semi-supervised domain adaptation approach is implemented that allows the fusion of simulated data with limited measurements of real-world structures, referring exclusively to the reference (healthy) state. By exploiting domain-adversarial training, the predictive performance with real data is significantly improved against conventional deep neural network approaches. This showcases the potential of domain adaptation for damage detection and characterization in real buildings, for which data collected in damaged states is almost never available. Adaptation favors transfer and thus application to a large number of buildings, alleviating the need for structural information and structure-specific modeling (Section 4).

2. Methodological framework

A main ingredient of the proposed approach lies in the development of an extensive dataset of nonlinear simulations of frame structures, which are representative of historic masonry buildings. To this end, a parametric nonlinear frame model is established. Initially, a thorough comparison of the damage predictive performance of individual features is conducted, based on the numerical simulations. Furthermore, ML damage classifiers that fuse multiple DSFs are tested. Finally, in order to enhance the generalization of the knowledge obtained from
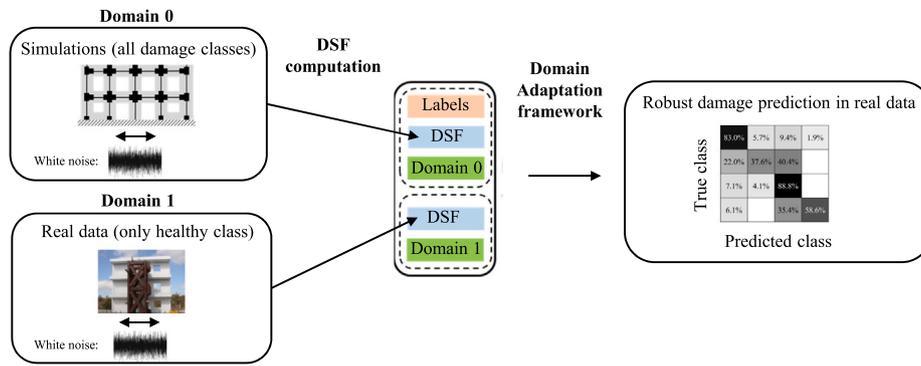
Fig. 1. Overview of the domain adaptation framework for robust damage prediction in real structures, based on simulations and on limited healthy data from the monitored structure.

training on simulated systems to real structures, a domain adaptation framework is proposed. As illustrated in Fig. 1, the framework involves training on simulations and limited data from the real structure, characterizing exclusively the healthy state.

2.1. Nonlinear parametric model of a generic building

The simulated data were generated using a parametric two-dimensional frame model, implemented in the application programming interface (API) of the commercial software SAP 2000 (v.23) [55]. The generated frame models represent the facades of conventional masonry buildings and follow the equivalent frame (EF) approach [56,57]. EF models are selected for their ease of assembly and their ability to lump nonlinearity in a computationally efficient manner, which is required to conduct a large number of simulations. In existing masonry buildings, the facade walls contribute predominantly to the global lateral stiffness of the structures. The regular disposition of openings further justifies the segmentation of masonry walls into spandrels and piers, with overlapping regions modeled with rigid offsets [56]. The free length of the piers and spandrels forms the deformable part of the wall and is modeled as a Timoshenko beam.

The modeling principles of the two-dimensional building geometry are schematically illustrated in Fig. 2. Subsequent seismic evaluation is limited to in-plane actions. The geometry of the walls is parameterized by changing the amount of floors (n) and bays (m), the height of the ground floor (h_{GF}), the height of the upper floors (h_{RF}), and the geometrical dimensions of all spandrels (l_{bi}, h_{bi}, t_{bi}) and piers (l_{wi}, h_{wi}, t_{wi}). The bounds of the uniform ranges of the geometric properties were selected to be representative of typical Swiss masonry buildings and are reported in Table 1. In addition, several material properties are considered as uncertain: the modulus of elasticity of masonry, E_{mas}, affects the lateral load-resisting behavior in both the elastic and the nonlinear regimes [58]. Given the uncertainty related to the equivalent elastic properties of masonry [59,60] and to the stiffness reduction during seismic events, a wide uniform range is chosen between 1 GPa and 4 GPa for uncracked conditions (Table 1). Accounting for the stiffness reduction due to cracking during seismic events, the modulus of elasticity is reduced by 50% [61–63]. The nonlinear behavior of masonry is lumped into hinges at the edges and in the middle of the elastic parts of piers and spandrels. A schematic representation of the hinge positions and capacity curves is given in Fig. 2b–c. The strength criteria for the nonlinear hinges are formulated according to Lagomarsino et al. [56]. The compression strength of masonry in the vertical direction f_k is considered linearly related to E_{mas}, as prescribed in the Swiss building codes [63]:

$$f_k = E_{mas}/1000 \tag{1}$$

In the absence of specific guidelines for horizontal compression strength, $f_{hk} = 80\% f_k$ is assumed. Although the shear and moment capacity of masonry depend on the acting axial loads [56],

Table 1
Parameters of the EF model.

Parameter	Unit	Min	Max
Number of floors (n)	–	2	5
Number of pier axes (m)	–	3	6
Height ground floor (h_{GF})	m	2.75	3.2
Height rest floors (h_{RF})	m	2.75	2.75
Wall length (l_w)	m	1	2.5
Beam length (l_o)	m	1	2.5
Wall and beam thickness (t_w, t_b)	m	0.2	0.2
Beam height ground floor ($h_{b,GF}$)	m	1	2.2
Beam height rest floors ($h_{b,RF}$)	m	1	2.2
Masonry E-modulus (E_{mas})	GPa	1.5	4
Masonry unit weight (w_{mas})	kN/m³	16	18
Masonry Poisson ratio (v_{mas})	–	0.2	0.2
Masonry shear strength (f_{v0k})	kN	100	200
Additional distr. loads (q_{distr})	kN/m	8	12
Viscous damping	%	1	2

the characteristic shear strength without compression (cohesion), f_{v0k}, is considered variable in the range of 0.1 MPa–0.2 MPa, according to Eurocode [64]. Following typical code-based seismic assessment approaches, compression and shear strength values are further reduced by a safety factor equal to 2 [63]. The maximum drift that each structural element can sustain is defined through the ultimate inter-story drift, δ_u, which is set equal to 0.4%, as suggested by the Swiss building codes [63]. The additional mass, beyond the self-weight of the structure, is modeled as uniformly distributed loads (q_{distr}) in the range of 8 kN/m–12 kN/m, applied to all spandrels.

In the absence of data justifying a more informed distribution, all parametric quantities are considered to follow a uniform distribution, within the ranges summarized in Table 1. A set of 4032 random samples is generated to perform nonlinear static and dynamic analyses.

2.1.1. Simulator data

Initially, a static nonlinear pushover analysis is performed on each structural realization. The structure is pushed in both the positive and negative directions by controlling the average displacement at the roof level, resulting from a lateral force distribution that is proportional to the modal shape of the first bending mode. Subsequently, a nonlinear dynamic analysis is conducted by applying one horizontal component of a historical ground motion to the base of the structure, where fixed boundary conditions are applied. The selected ground motion corresponds to the x-component of the 1981 Alkion earthquake in Greece (Station: ST121, waveform: #333) with a PGA of 0.23 g [65] (Fig. 3). Increasing DSs are generated for each model configuration by scaling the ground motion to nine amplitudes: $GM_{scale} = 0.2, 0.4, 0.5, 0.6, 0.7, 0.8, 0.9, 1.0, 1.2$, corresponding to: PGA = 0.046 g – 0.276g. All time–history analyses are assumed to begin from the pristine (healthy) state. Following each ground motion, a low-amplitude
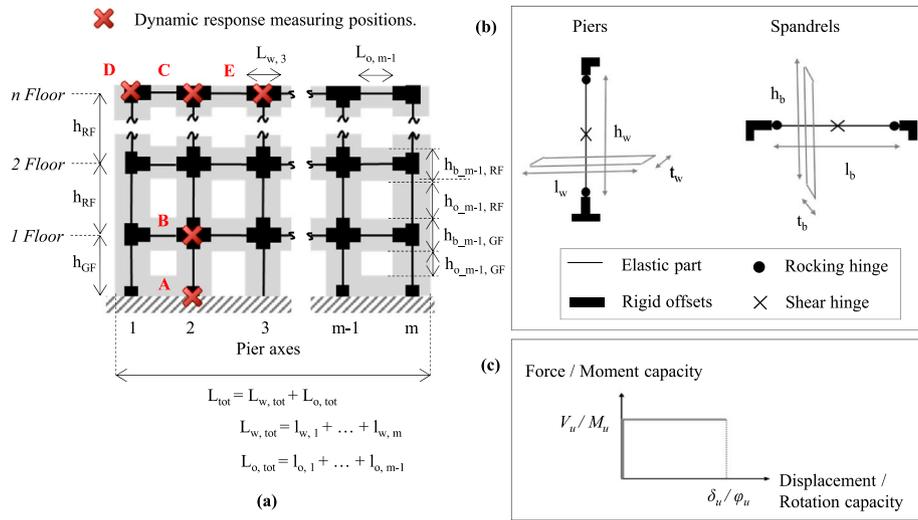
Fig. 2. Equivalent frame model: (a) Generic representation of the parametric model, (b) Discretization and nonlinear hinge positions, (c) Backbone curve formulation for the nonlinear hinges. The strength criteria for the nonlinear hinges are formulated according to Lagomarsino et al. [56].
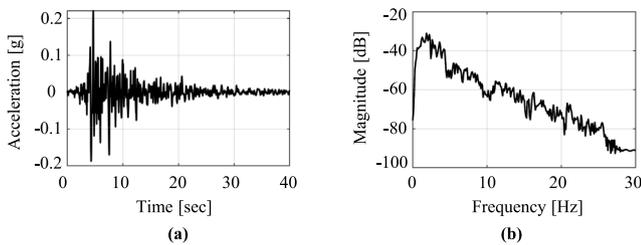

Fig. 3. The Alkion 1981 ground motion. Response depicted in time-domain (a) and in frequency-domain (b).

Fig. 4. (a) Definition of empirical DSs on the basis of a bilinear approximation of a push-over curve, (b) Damage state distribution of the dataset, (c) Data split for training, validation and test.

white-noise (WN) excitation (with frequency content between 1 Hz and 40 Hz), with a root mean square (RMS) amplitude of 0.01 g is applied at the bottom of the structure. The selected frequency range covers the natural frequencies of low- and medium-rise masonry and concrete structures, which typically range from 2 Hz to 15 Hz [66]. This WN excitation simulates post-earthquake low-amplitude vibrations. All damage-sensitive features (DSFs) are computed during the WN excitation that follows the strong ground motions. As a result, the derived DSFs evaluate changes in the dynamic characteristics due to residual damage. The effect of ground motion variability on the produced damage falls outside of the scope of this work, which focuses on the comparison of damage detection approaches in a wide range of realistic structural configurations. In addition, the structure remains quasi-linear under the simulated low-amplitude WN and thus, the influence of the WN amplitude on the computed DSFs is considered minor. Assuming such a perfect WN excitation may not cover all real-world cases but is deemed acceptable for the simulation.

2.2. Damage labels

For the characterization of the severity of the damage sustained by the structure, an empirical mapping scheme based on the ARD ratio is employed. By considering the bilinear approximation of the capacity curve obtained from static nonlinear analysis (using the N2 method proposed by Fajfar [67]), the idealized yield displacement is used to define thresholds for the distinctive global DSs (see Fig. 4a):

- Healthy state: maximum transient displacement below 70% of the yield displacement
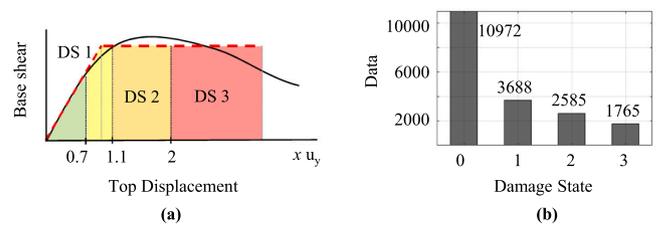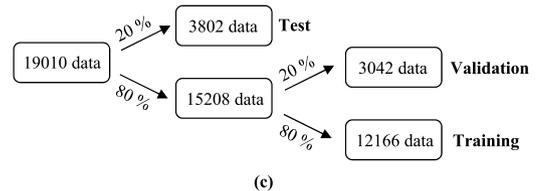- Slight damage: 70%–110% of the yield displacement

- Moderate damage: 110%–200% of the yield displacement
- Extensive damage: > 200% of the yield displacement

Current practice in regional seismic vulnerability and risk assessment adopts the ARD to characterize the severity of the damage, often comparing it with thresholds established with an idealized version of the capacity curve [3,68–70]. However, while most formulations include an estimate of the ultimate displacement capacity, the corresponding value is rather volatile and affected by several underlying modeling assumptions, as well as the definition of the ultimate displacement capacity itself. In addition, with the visual inspection of near-collapse building states being rather straightforward, monitoring-driven quantification is not contributing much to the assessment of such cases. Here, assessment of lower – less obvious DSs – is addressed and these cases are defined on the basis of the bilinearized yield point. This uncertainty is reflected in the reduced predictive performance with respect to intermediate damage classes (Section 3). However, the definition of a unique damage threshold lies outside the scope of this work, as the proposed framework for damage characterization based on DSFs is independent from the exact definition of the damage classes.

The minimum yield displacement between positive and negative directions is considered to define the DS thresholds. The maximum
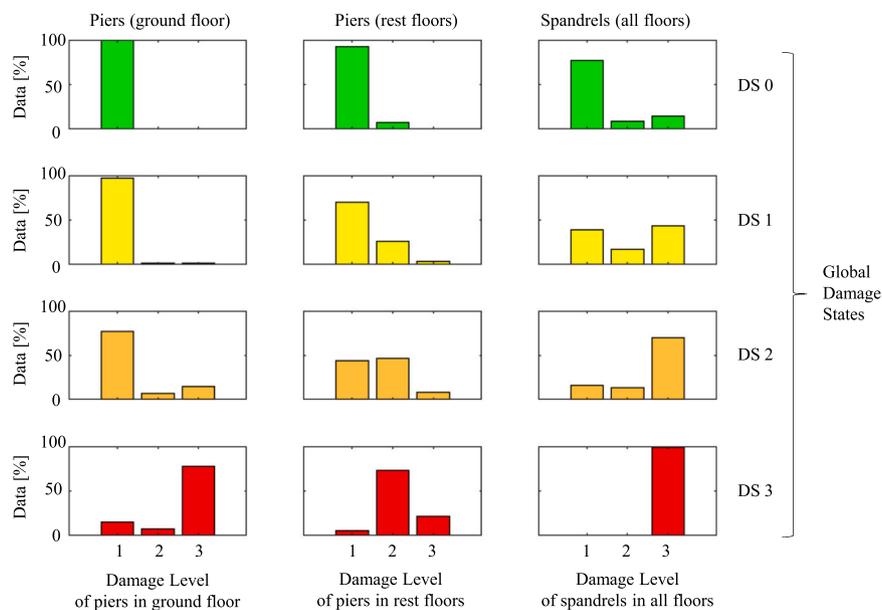
Fig. 5. Damage level distribution per element group for each global damage state (DS0 to DS3). All 19010 data are considered.

average roof drift (MRD) is reached during each time-series analysis is used to attribute global DSs, by comparison with damage thresholds defined on the pushover curve of each model configuration. Such global DSs exclude separation between global and local failure modes (such as out-of-plane and soft-story mechanisms) and coincide with the observed damage patterns that feature distributed damage instances in all floors (Fig. 5). Considering all model configurations and DSs, a total of 19010 data points are generated. The distribution of DSs is provided in Fig. 4b. Although healthy data comprise over 55% of the dataset, the rest of the DSs are roughly balanced. This dataset is randomly shuffled and divided into training (64%), validation (16%) and test (20%) sets, as illustrated in Fig. 4c.

The actual damage patterns that correspond to the empirically defined DSs are illustrated after grouping the structural elements into three categories: piers in the ground floor, piers in the remaining floors, and spandrels in all floors. For the visualization of damage at element-group level, a conservative assumption is followed: individual spandrels and piers are considered damaged as soon as at least one of the rocking or shear hinges (Fig. 2) yields. By counting the percentage of damaged elements in each group, the damage levels are estimated as follows:

- **Group Damage Level 1**, if 100% of the elements are healthy.
- **Group Damage Level 2**, if $\geq$ 75% of the elements are healthy
- **Group Damage Level 3**, if < 75% of the elements are healthy.

Fig. 5 compares the damage level of the three element groups with the global DS attributed to the structure, based on the analyses results from all simulated building configurations. For the globally healthy state (DS 0), all the piers are healthy, while in few cases more than 25% of the spandrels experience a nonlinear response. In more than 40% of DS 1 cases the amount of damaged spandrels is significant (damage level 3), while in 20% of the DS 1 cases piers above the ground floor reach the plastic range, as the lower axial forces result in reduced lateral capacity [56]. For global DS 2, the majority of the cases present heavily damaged spandrels, while the number of damaged piers above the ground floor increases as well. In global DS 3, spandrels are damaged in all cases. In almost all cases the piers above the ground floor are partially damaged, while in 80% of the cases a significant part of the piers in the ground floor reaches the nonlinear range as well. Overall, damage initiates in the spandrels, progresses to the piers in the upper floors, and reaches the piers in ground floor at later global DSs.

2.3. Engineering demand parameters

Thresholds based on EDPs are typically used to separate DSs and thus form the cornerstones of fragility functions that link earthquake intensity with the probability of reaching a given DS [52]. Typical EDPs are the maximum inter-story drift ratio (ISD_{max}), possibly limited to the ground floor (ISD_{gf}). In addition, the MRD is evaluated, as it is used to define global DSs for each individual model configuration and is often used in regional risk assessment [51]. As EDPs are intrinsically chosen to correlate well with damage, monitoring these quantities would facilitate precise loss assessment in the aftermath of earthquakes. However, dynamically measuring displacements is challenging in real structures, especially in cases of stiff, low-rise masonry buildings. Vibration monitoring is mainly based on sensors that measure accelerations or velocities. As the calculation of displacements through numerical integration of the measured accelerations lacks consensus with the actual displacements [71], extraction of DSFs from measured acceleration or velocity signals is more practical.

2.4. Damage-sensitive features

For the purposes of this work, an extensive set of features is computed in the time and frequency domains. To define a generic feature space that is independent from the individual characteristics of each model configuration, the selected features are computed exclusively at the positions A to E, depicted in Fig. 2a. These sensor positions cover the ground, the first floor, and the top floor of the modeled structure. The typical frequency range that includes the main modes of vibration of buildings is 1 Hz–30 Hz. Prior to computing features, acceleration signals are pre-processed and band-pass filtered between 1 Hz–40 Hz using a Butterworth filter to mitigate the effect of noise due to spurious vibrations beyond this range. As all frequency-domain features are computed in narrow frequency ranges within the pass-band, the classification accuracy is not expected to be sensitive to the type of filter. All DSFs are extracted from WN excitation, as described in Section 2.1, and are summarized in Table 2. Additional features describing the geometrical configuration are summarized in Table 3. Finally, selected physical quantities of the healthy building state that can be retrieved from vibration monitoring before a damaging earthquake, such as the natural frequencies of the building and indirectly inferred elastic properties, are summarized in Table 4. It is noted that,

Table 2
List of deployed acceleration-based DSFs.

ID	DSF	Domain	Pos.	Notes
1–3	TAC	Freq.	A-B	fr. ranges 1–3
4–6	TAC	Freq.	B-C	fr. ranges 1–3
7	RMS	Time	A-C	RMS_C/RMS_A
8	AR_1	Time	A-C	1st AR param.
9	ED_1	Time	A-C	ground floor
10	ED_2	Time	B-C	rest floors
11	TAC_{beam}	Freq.	C-D	fr. range 3
12	TAC_{beam}	Freq.	C-E	fr. range 3
13–15	$TAC_{beam,GF}$	Freq.	B-D	fr. ranges 1–3
16–18	$TAC_{beam,GF}$	Freq.	B-E	fr. ranges 1–3
19–21	TAC_{TB}	Freq.	A-C	fr. ranges 1–3
22	$CURV_{GF}$	Freq.	A-B	ground floor
23	$CURV_{RF}$	Freq.	B-C	rest floors

Table 3
List of geometric configuration features (CFs) with reference to Fig. 2.

ID	CFs	Unit	Notes
1	L_{tot}	m	Total length
2	t_w	m	Wall thickness
3	n_{piers}	–	Number of pier axes
4	$L_{w,tot}$	m	Total wall length
5	$L_{w,av}$	m	Average wall length
6	$L_{w,min}$	m	Minimum wall length
7	$L_{w,max}$	m	Maximum wall length
8	$L_{o,tot}$	m	Total opening length
9	$L_{o,av}$	m	Average opening length
10	$L_{o,min}$	m	Minimum opening length
11	$L_{o,max}$	m	Maximum opening length
12	$Op_{perc,GF}$	%	Relative area of openings in ground floor
13	$Op_{perc,RF}$	%	Relative area of openings in rest floors
14	n_{floors}	–	Number of floors
15	h_{GF}	m	Height ground floor
16	h_{RF}	m	Height rest floors

Table 4
List of monitoring-based inferable features (MFs)

ID	MFs	Unit	Notes
1	E_m	GPa	Masonry E-modulus
2	w_m	kN/m^3	Masonry unit weight
3	q_{distr}	kN/m	Distributed load per floor
4	F_1	Hz	1st modal freq.
5	F_2	Hz	2nd modal freq.
6	F_3	Hz	3rd modal freq.

while the natural frequencies (features 4–6) can be obtained from continuous ambient-vibration monitoring using conventional operational modal analysis techniques, material and load parameters (features 1–3) require model identification approaches that are not trivial. The uncertainties in deriving all six features are omitted in this analysis, which evaluates an upper limit of the contribution of these features.

2.4.1. Time domain features

Time domain features are defined to capture changes in response characteristics due to permanent structural damage. The response is evaluated at the top of the ground floor and at the top of the structure (points B and C per Fig. 2) under low-amplitude WN excitation. To reduce the influence of the frequency content of the WN excitation, the response at points B to E is normalized with respect to the absolute response at point A.

The RMS amplitude of the response at the top of the structure, normalized to the input at the ground level, indicates global changes in the amplitude of the propagated signal. To capture changes in higher-order characteristics, a four-order autoregressive model (AR) is trained to fit the response at the top (point C), normalized to the input at the ground level, and the parameters of the AR model are included

as DSFs. The choice of limiting the AR model to the first four orders was purely driven by heuristics and the change in performance with lower or higher order terms has not been studied, yet without loss of generalization other orders could be included in the feature set. Finally, in an attempt to formulate a feature that captures changes in energy flow through the structure, approximations of the velocity ($\hat{v}$) and displacement response ($\hat{u}$) are derived by integrating the acceleration signal in the time domain. Prior to integration, the acceleration signal is band-pass filtered between 1 Hz and 40 Hz through a 4th order Butterworth filter. The computed approximations are normalized to the corresponding approximations of velocity and displacement at the ground level. A quantity inspired by the kinetic energy ($\hat{E}_{kin}$) is calculated by integrating the square of the relative velocity response, while a proxy inspired by the potential energy ($\hat{E}_{pot}$) is derived by integrating the product of the relative displacement and the absolute acceleration response.

$$\hat{E}_{kin} = \int \hat{v}^2 \, dt \tag{2}$$

$$\hat{E}_{pot} = \int \hat{u} \cdot a_{abs} \, dt \tag{3}$$

By summing the above approximations, the quantity $\hat{E}$ is defined:

$$\hat{E} = |\hat{E}_{kin}| + |\hat{E}_{pot}| \tag{4}$$

These approximate numerical integration results serve exclusively to the formulation of the DSF and are not intended to capture the real displacement or velocity response, given the inherent loss of information. Taking the points A and B as a reference (Fig. 2a), two DSFs are defined, based on the relative displacement and velocity evaluating the output at points B and C, respectively. By normalizing $\hat{E}$ in the current state ($\hat{E}^d$) to the reference state ($\hat{E}^r$), the following DSF is formulated:

$$ED = \frac{\hat{E}^r - \hat{E}^d}{\hat{E}^r} \tag{5}$$

2.4.2. Frequency domain features

The acceleration signals are converted to the frequency domain by implementing Welch's method [72] with 50% overlapping segments windowed with a Hamming window. The aim of the frequency-domain features is to provide a comparison between the pristine and the potentially damaged building state, as opposed to identifying the exact frequency or transmissibility. In this latter case, more advanced spectral analysis techniques would be more suitable, as elaborated in [73]. Transmissibility-based criteria have been proposed for the detection and localization of damage based on output-only data [74]. The transmissibility function between points a and b of an elastic system can be defined as the ratio of the complex amplitude of the system responses in the frequency domain, which can be expressed as a fraction of power spectral densities:

$$T_{a,b}(\omega) = \frac{X_a(\omega) \times X_b(\omega)}{X_b(\omega) \times X_b(\omega)} = \frac{G_{a,b}(\omega)}{G_{b,b}(\omega)} \tag{6}$$

where $X_a(\omega)$ is the complex amplitude of the system response at the point a, as a function of the angular frequency ω, and $G_{a,b}(\omega)$ is the cross-spectral density between the points a and b. By considering the transmissibility function between points a and b at healthy state as reference, the Transmissibility Assurance Criterion (TAC) evaluates the goodness of fit between transmissibility in the damaged and reference state in a pre-defined frequency range [75]:

$$TAC_{a,b} = \frac{[(T^d)^T(T^r)]^2}{[(T^d)^T(T^d)][(T^r)^T(T^r)]} \tag{7}$$

where T^r and T^d represent the truncated transmissibility vectors in reference and damaged conditions. For the truncation of the transmissibility function, three frequency ranges have been considered: 3 Hz – 8 Hz, 8 Hz – 15 Hz and 15 Hz – 22 Hz. By evaluating the transmissibility

between different points of the structure, several TAC features have been defined, as reported in Table 2. Another frequency domain feature that is defined between two points of the structure and relates to the modal curvature, is expressed as follows:

$$CURV_{a,b} = \frac{\phi_b - \phi_a}{h_{a,b}} \tag{8}$$

where ϕ_a represents the normalized modal displacement at point a and $h_{a,b}$ the distance between the points a and b.

2.5. Fragility functions

A fragility function is a mathematical function that expresses the cumulative probability of reaching a limit state as a function of an intensity measure (IM), typically characterizing the ground motion intensity [76]. The most common form is the log-normal cumulative distribution function (CDF):

$$P(\text{DS} \mid \text{IM}) = \Phi\left(\frac{\ln(\text{IM}/\theta)}{\beta}\right), \tag{9}$$

where $P(\text{DS} \mid \text{IM})$ is the probability that ground motion with intensity measure IM will cause the structure to reach the limit state DS, Φ is the standard normal cumulative distribution function with median θ and standard deviation β. The parameters of the fragility function, β and θ, are uniquely defined for each DS.

The probability of reaching a DS for a given IM level can be estimated as the fraction of records, for which the damage-defining variable, for instance roof drift ration, falls in a defined interval. To fit a log-normal cumulative distribution function, the median and standard deviation must be estimated, for example, using the maximum likelihood method [77,78]. Although log-normal distributions are the most common choice for fragility functions, beta functions may also be used [79]. Once established, a fragility function enables the prediction of the probability of a building to be in a given DS using the IM, as shown in Eq. (9). The same procedure can be used to fit fragility functions based on either EDPs or DSFs, which can be measured directly. Fragility functions, based on IMs, are widely used in rapid loss assessment, especially at regional level [80,81].

2.6. Supervised machine learning approaches

Provided the availability of labeled data, supervised classification schemes have demonstrated good performance in damage detection and characterization tasks: by fusing information from multiple features, classifiers produce robust damage predictions. However, in real-world SHM applications limited labeled data from damaged conditions undermine a direct application of supervised damage classification schemes. Yet, increased computational capabilities enable the simulation of large volumes of data from high-fidelity computational models. In this work, two ML architectures are deployed, Convolutional Neural Networks (CNNs) and Decision Trees (DTs). The performance of the algorithms is evaluated by means of predictive classification performance in the test set (Section 2.2). Three different sets of features are considered: (i) only DSFs (see Table 2), (ii) DSFs + geometric configuration features (CFs per Table 3), and (iii) DSFs + CFs + monitoring-inferred structural features (MFs per Table 4). The split of the data into training, validation, and test sets is described in Section 2.2.

2.6.1. XGBoost architecture

Information from various features can be used to perform supervised learning of a robust damage classifier, namely gradient-boosted DTs [82], as implemented in the XGBoost algorithm [83]. While traditional DTs use hard conditions to classify data into target labels, the XGBoost algorithm parallelizes the training of multiple DTs. For a given training set with n samples and m features, a tree ensemble model

(Fig. 6a) uses K decision trees to derive predictions $\hat{y}_i$ corresponding to the real class y_i as follows:

$$\hat{y}_i = \sum_{k=1}^{K} f_k(\boldsymbol{x}_i), f_k \in F; \tag{10}$$

where $\boldsymbol{x}_i$ represents the feature vector, f_k is the kth tree function, and F refers to the tree space. The optimal set of functions is derived by minimizing the following regularized objective:

$$L = \sum_{i=1}^{m} l(\hat{y}_i, y_i) + \sum_{k=1}^{K} \Omega(f_k) \tag{11}$$

The first term, l, represents a differentiable convex loss function and accounts for the prediction accuracy. The second term, Ω, is a regularization term that penalizes the complexity of the model, thus preventing overfitting. This regularized objective function is designed to select a model that employs simple and predictive functions. However, including functions as parameters prevents the application of traditional optimization methods in Euclidean space. Thus, the model is trained in an additive manner, by adding tree functions and keeping those that improve the predictive accuracy without increasing the complexity significantly. The detailed derivation of the gradient tree boosting algorithm is documented in Chen and Guestrin [83]. For the implementation of the algorithm, the open source python library https://xgboost.readthedocs.io/ has been deployed, by adopting the default values for the hyperparameters. Logistic regression has been used as an objective function, while the validation metric is the negative log-likelihood on multi-class classification error rate: wrong cases/all cases.

2.6.2. Convolutional neural network architecture

Provided extensive labeled datasets for training and validation, neural networks have demonstrated very high performance in damage classification tasks, by combining information from multiple features [31,34]. Typically, CNNs are deployed directly on time-series measurements [84] or picture data [85]. In this work a CNN architecture is deployed on the pre-computed features (see Section 2.4), as illustrated in Fig. 6b. The architecture comprises a latent-space feature extractor and a damage classifier. This separation is compatible with the domain adaptation framework introduced in Section 2.7. The generic layer structure of the feature extractor contains an input layer with the length of the initial feature space and a variable number of 1D CNN layers with a kernel size of 3, followed by dropout regularization and a hyperbolic tangent activation function (tanh). Finally, a dense layer (fully connected) with variable output length is added for the computation of the latent features. The number of convolutional layers and the length of the latent feature space are tuned through a grid search within the range described in Table 7.

The latent-space features produced by the feature extractor are provided as input to the damage classifier, which consists of four dense layers that output the predicted damage class. The size of the dense layers has been selected following a grid search in the range 50 to 1000 neurons. The model output in terms of the predicted damage class is provided through a softmax activation function. The detailed architectures of the feature extractor and the damage classifier are reported in Tables 5 and 6, respectively. The Adam optimizer is used, and a grid search is conducted, in order to tune the hyperparameters of the model. Although more efficient methods for the estimation of the optimal set of hyperparameters exist [86,87], this task lies beyond the scope of the present work. The ranges of the hyperparameters and the selected values are summarized in Table 7.

2.7. Domain adaptation framework

Domain adaptation aims to improve the predictive performance of a classifier in the target domain, for which no labels are available,
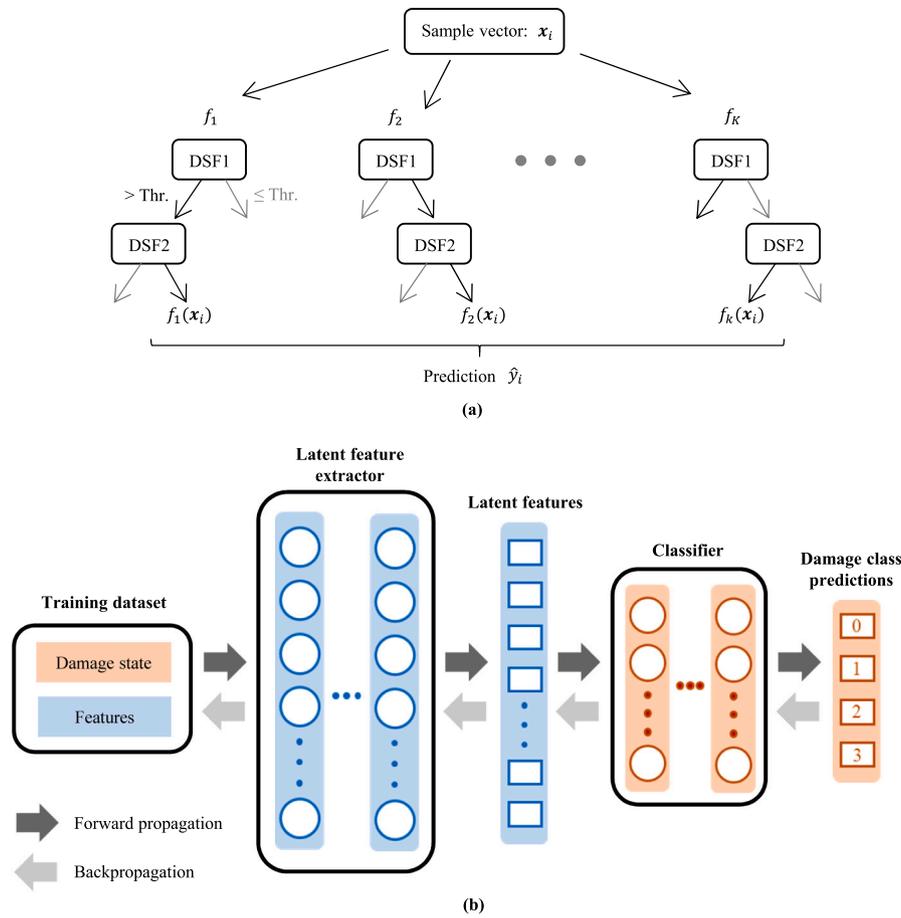
Fig. 6. Schematic representation of (a) a decision tree ensemble model, (b) the Neural Network classifier architecture.

Table 5
Selected architecture for the feature extractor.

ID	Layer	Output size	Activation	Dropout
1	Input	n. of features		
2	1D Conv.	n. of features	tanh	–
3–6	1D Conv.	n. of features	tanh	25%
7	Dense	200	tanh	50%

Table 6
Selected architecture for the damage classifier.

ID	Layer	Output size	Activation	Dropout
1	Input	200		
2	Dense	400	tanh	20%
3	Dense	200	tanh	20%
4	Dense	50	tanh	20%
5	Dense	n. of classes	softmax	

Table 7
CNN hyperparameters ranges and selected values.

Parameter	Min	Max	Selected value
N. of CNN layers	2	6	4
Latent space length	20	300	200
Learning rate	0.0001	0.01	0.001
Batch size	4	64	8

by training the classifier with labeled data from the source domain and limited unlabeled data from the target domain. For instance, the source domain could consist of a simulation model, and the target domain a real-world structure. Here, a Domain Adversarial Neural Network approach (DANN [46]) is implemented, which capitalizes on Generative Adversarial Networks (GAN [88]). The adopted DANN architecture, illustrated in Fig. 7, comprises three elements: a latent-space feature extractor (FE) that maps the input to a D-dimensional latent feature vector (f_l), a damage classifier (DC) that maps f_l to a prediction of DS, and a domain discriminator (DD) that maps f_l to a binary domain label. By denoting the trainable parameters of each component with θ, a unified objective function can be formulated:

$$E(\theta_{FE}, \theta_{DC}, \theta_{DD}) = L_y(\theta_{FE}, \theta_{DC}) - \lambda \cdot L_d(\theta_{FE}, \theta_{DD})$$
$$(\hat{\theta}_{FE}, \hat{\theta}_{DC}) = \arg \min_{\theta_{FE}, \theta_{DC}} L(\theta_{FE}, \theta_{DC}, \hat{\theta}_{DD})$$
$$\hat{\theta}_{DD} = \arg \max_{\theta_{DD}} L(\hat{\theta}_{FE}, \hat{\theta}_{DC}, \theta_{DD}) \tag{12}$$

In Eq. (12), the first part (L_y) minimizes the label prediction loss, as conventionally done for supervised ML approaches. The second part (L_d) is an adversarial loss that behaves differently in forward and backward propagation. In forward propagation, the domain prediction loss is maximized. The weights of the feature extractor are trained so that the latent feature space remains domain-invariant. In back-propagation, the domain prediction loss is minimized. The weights of the domain discriminator are trained, with the goal of maximizing the precision of predicting the origin of the latent-space features. The parameter λ controls this transition and is materialized by introducing a gradient reverse layer (GRL) between the feature extractor and the damage classifier [46]. The adaptation parameter λ is initiated at 0 and is progressively increased to 1 along the training epochs, through the following schedule:

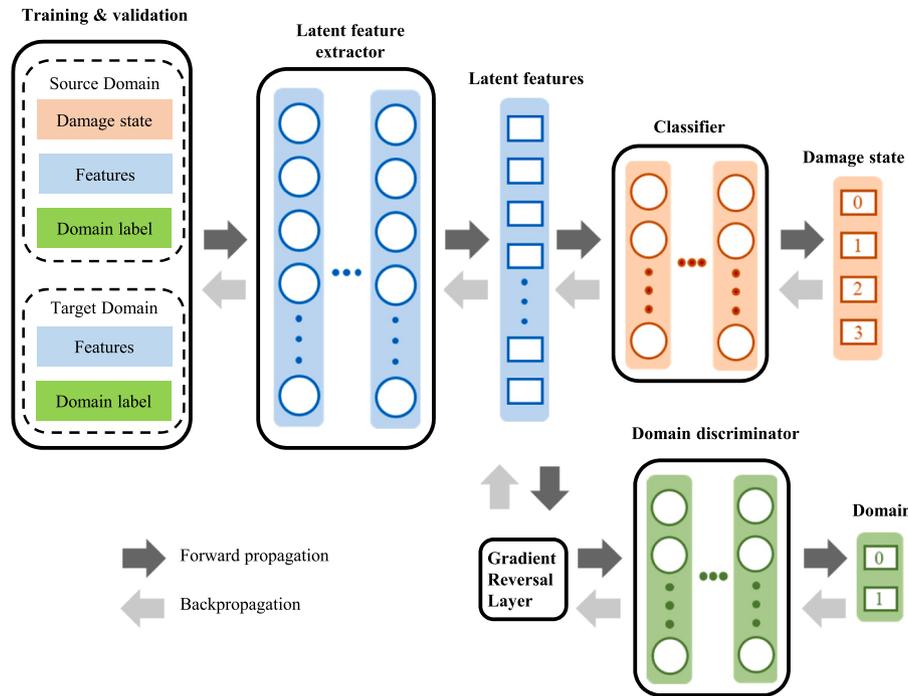$$\lambda = \frac{2}{1 + e^{-10 \cdot p}} - 1 \tag{13}$$

Fig. 7. Schematic representation of the generic architecture of a DANN model.

Table 8
Selected architecture for the domain-discriminator.

ID	Layer	Output size	Activation	Dropout
1	Input	200		
2	Dense	100	tanh	20%
3	Dense	50	tanh	20%
4	Dense	2	softmax	–

where p is the training progress linearly changing from 0 to 1. This strategy prevents the domain classifier from being sensitive at the early stages of the training procedure [46].

The generic layer structure of the feature extractor and the damage classifier is described in Section 2.6.2 and summarized in Tables 5 and 6. The domain discriminator contains three dense layers with variable lengths, leading to the number of damage classes. The output length of the dense layers has been selected after a grid search in the range 50 to 1000. The model produces a binary prediction of the original domain, through a softmax activation function. The detailed architecture of the domain discriminator is reported in Table 8.

3. Simulated data of earthquake damage

3.1. Damage prediction based on fragility functions

The damage prediction performance of individual EDPs and DSFs is evaluated with the simulation data presented in Sections 2.1 and 2.2. For each feature, fragility functions, describing the probability of reaching the respective DSs (Fig. 4a), are derived by considering only the training data (Fig. 4c) and by fitting a log-normal distribution to the empirical CDF, as explained in Section 2.5. The predictive performance is evaluated with the test data by computing the predictive accuracy, as a function of true positives (TP), false positives (FP), true negatives (TN), and false negatives (FN):

$$Accuracy = \frac{TP + TN}{TP + TN + FP + FN} \tag{14}$$

Furthermore, a less strict accuracy metric, termed "soft" accuracy, is computed and accepts predictions that yield ± 1 damage class from

reality. The predictive performance is illustrated with confusion matrices, where each row contains the normalized or absolute number of instances in an *actual* damage class and each column contains the corresponding number of instances in a *predicted* damage class.

Fragility functions evaluate the probability that the structure reaches a specific DS based on the value of a single IM. Here, the peak ground acceleration (PGA) is considered as IM. Fragility functions for all damage grades are derived using training data (Fig. 4c) and plotted in Fig. 8. While there is a clear distinction between healthy state (DS 0) and damaged states (DS 1–3), the predictive accuracy is very poor (below 50%). As illustrated in the corresponding probability density functions (10a), the probability of DS 1 is always lower than the probability of DS 0 and 4, while the probability of DS 2 exceeds DS 3 for higher PGA values. This is reflected in the confusion matrices evaluated in the test data (Fig. 8), where the prediction of DS 1 is missing and most of the data belonging to DS 2 are misclassified. It is noted that unlike in regional seismic risk applications [89], no post-processing of the fragility functions is made to avoid such crossing of fragility functions that describe increasing DSs and no hard assumptions that usually help avoiding such behavior, such as equal standard-deviation for all DSs, is taken. Overall, the poor predictive performance indicates that information solely from the ground, expressed through IMs, is insufficient to provide robust damage estimates. While IM-based fragility functions – often derived with single degree of freedom systems (SDOF) – reflect the state of practice for seismic risk analyses at regional scale, the poor correlation of the studied IM with the predicted DSs underline their limited structure-specific applicability to complex multi-degree of freedom systems (MDOF). In Fig. 8a to c, the fragility curves are created based on three different subsets of the training data, considering exclusively two-floor configurations, exclusively four-floor configurations, and the entire training set that comprises buildings with two to five floors. The predictive accuracy is tested in the corresponding subsets of the test set, yielding similarly low accuracy levels in all cases. This observation confirms that the predictive performance of IM-based fragility functions remains poor, even when the number of floors is fixed.

EDPs are structural response quantities that typically rely on displacements to estimate structural (and non-structural) damage. Measuring displacements directly in real buildings is challenging and the
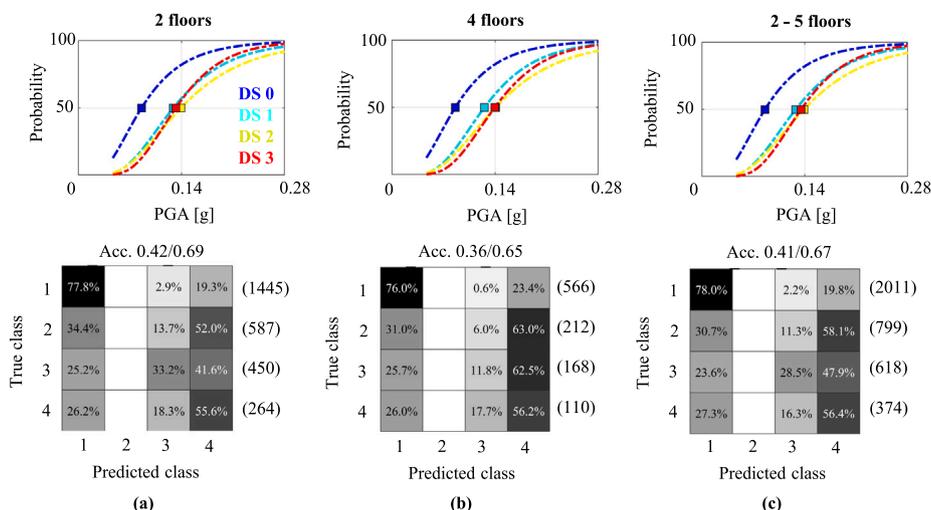
Fig. 8. Fragility curves for all DSs based on training data (top) and confusion matrices reflecting the accuracy when applied to test data (bottom). The *x*-axis of the fragility curves corresponds to PGA. Model configurations: (a) 2-floor buildings, (b) 4-floor buildings and (c) 2- to 5-floor buildings.

related costs almost prohibitive, especially in low- to medium-rise masonry buildings with displacements in the order of millimeters. However, assuming displacement measurements are available, fragility functions are developed that depend directly on three characteristic EDPs, namely the MRD, ISD_{max}, and ISD_{gf}, as described in Section 2.3. Fig. 9a illustrates the fragility functions for ISD_{gf}, which produced the best accuracy, resulting from the training dataset that includes only 2-floor configurations. The confusion matrix evaluated in the test set displays a 70% accuracy and 97% soft accuracy (accepting ±1 damage classes). While the damage labels for each individual model configuration are defined based on the corresponding capacity curve (Section 2.2), the fragility functions are developed collectively, considering the training set (Fig. 4c) that includes data from all model configurations. As a result, the accuracy for individual structures is not perfect, which is attributed to the inevitable simplifications associated with SDOF systems that approximate the nonlinear characteristics of complex MDOF structures. Nevertheless, the fragility functions based on EDPs offer an upper bound to the accuracy of damage classification, in the idealized case of measurable displacements. Additionally, the soft accuracy indicates a clear separation between lower and higher DSs (DS 0 and DS 3 respectively, per Fig. 4). The increased confusion in DS 1 and 2 is attributed to the fact that the ISD_{gf} is sensitive to damage in ground floor, which mostly concerns DS 3 (Fig. 5). Fig. 9b contains the same information after including all available model configurations (with two to five floors) for both training and testing. Absolute accuracy drops to 66%, which is slightly less than in the previous case and indicates the increased uncertainty in the fragility curves when multiple model configurations are considered.

The same procedure is applied to all DSFs reported in Table 2, considering the complete training set that contains all building configurations. The predictive accuracy evaluated in the test set for each feature individually is reported in Table 9. The highest accuracy (56%) is achieved by DSF #7, which is the RMS amplitude of the normalized response at the top of the structure (Table 2). The corresponding soft accuracy is 91%. As expected, both the absolute and soft accuracy are lower than the ISD, although significantly higher than the IM. It is mentioned that all DSFs are computed on the basis of the acceleration response in the pre-defined positions mentioned in Fig. 2a and represent measurable features, assuming that the structure is instrumented with accelerometers.

Fig. 10 illustrates the probability density functions for all DSs by considering the PGA, the ground floor inter-story drift and the best performing DSF as damage indicators. For the case of PGA, the overlapping of the curves corresponding to global DSs above 0 reflects the

Table 9
Accuracy and soft accuracy (± 1 damage class) obtained from applying fragility functions to the test set. Fragility functions are formulated with respect to either intensity measures (IMs), engineering demand parameters (EDPs), or damage-sensitive features (DSFs). The maximum accuracy achieved for each category (IM, EDP, DSF) is highlighted in bold.

Type	ID	Description	Accuracy	Soft accuracy
IM	–	PGA	**0.41**	**0.67**
EDP	–	MRD	0.59	0.95
EDP	–	ISD_{gf}	**0.66**	**0.97**
EDP	–	ISD_{max}	0.59	0.95
DSF	1	see Table 2	0.52	0.84
DSF	2	see Table 2	0.52	0.83
DSF	3	see Table 2	0.47	0.79
DSF	4	see Table 2	0.52	0.85
DSF	5	see Table 2	0.52	0.83
DSF	6	see Table 2	0.47	0.79
DSF	7	see Table 2	**0.56**	**0.91**
DSF	8	see Table 2	0.49	0.83
DSF	9	see Table 2	0.51	0.83
DSF	10	see Table 2	0.52	0.83
DSF	11	see Table 2	0.47	0.79
DSF	12	see Table 2	0.48	0.79
DSF	13	see Table 2	0.45	0.88
DSF	14	see Table 2	0.50	0.83
DSF	15	see Table 2	0.47	0.79
DSF	16	see Table 2	0.46	0.89
DSF	17	see Table 2	0.50	0.83
DSF	18	see Table 2	0.48	0.79
DSF	19	see Table 2	0.53	0.85
DSF	20	see Table 2	0.53	0.83
DSF	21	see Table 2	0.48	0.79

inability of the IM to differentiate between damaged states based on the maximum probability principle. For the case of the ground floor inter-story drift and the best performing DSF, the distributions are separable and consistent with the increasing level of damage. The inevitable overlapping is the main source of confusion in the prediction of damage based on individual features. As different features are sensitive to different DSs, in the next section multiple DSFs are fused in order to improve the overall predictive performance.

3.2. Damage state prediction with supervised machine learning approaches

Two ML approaches, namely XGBoost and CNNs, are leveraged to fuse the information from multiple features. As described in Section 2.6, the input for both networks is a set of pre-computed features, the output is the prediction of the DS, while three different sets of features
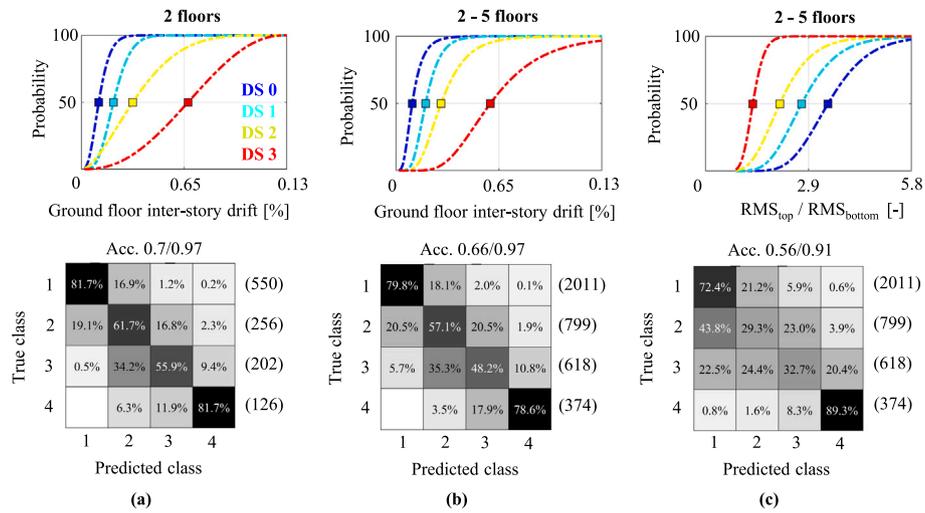
Fig. 9. Fragility functions derived from training data (top) and confusion matrices evaluated on test data (bottom). The *x*-axis corresponds to: (a) Inter-story drift at ground floor (only 2-story configurations), (b) Inter-story drift at ground floor (2- to 5-story configurations), (c) Best performing individual DSF (2- to 5-story configurations).
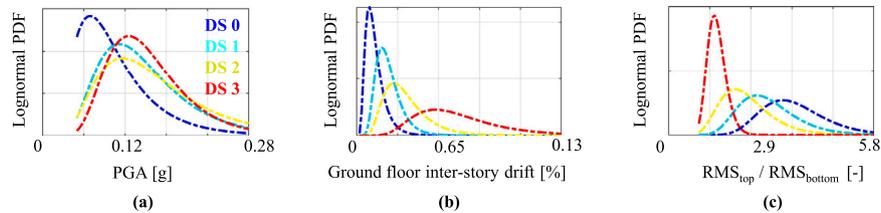

Fig. 10. Probability density functions for all DSs based on training data for all model configurations. The *x*-axis corresponds to: (a) PGA, (b) Ground floor inter-story drift and (c) Best performing individual DSF.

are considered. The results obtained for both classifiers on all three feature-combinations are summarized in Fig. 11.

Both architectures demonstrate significantly better predictive performance compared to fragility functions based on individual features. Considering only DSFs, the XGboost architecture yields 66% accuracy and 96% soft accuracy, which is comparable to the predictive performance of the ISD. This demonstrates that fused acceleration-based DSFs have the potential to yield predictive performance that reaches the level of hypothetically known ISD. Including geometric configuration features (CFs) increases the predictive accuracy to 70% and 97% (soft accuracy). In a step further, characteristic structural properties (MFs per Table 4) that are possible to infer through model updating frameworks [66] are considered. Although significant computational effort is required for this task, the improvement in terms of accuracy is only marginal (Fig. 11c). Overall, the predictive performance of the CNN architecture is consistently inferior to that of the XGBoost architecture. This is attributed to the limited amount of training data and to the ability of the XGBoost architecture to reduce overfitting through regularization.

Fig. 12 demonstrates the feature importance for the classification decisions of the XGBoost architecture for the three combinations of features tested. The normalized RMS amplitude and the TAC between points B and C (Fig. 2a) have the largest impact on the damage classification. This highlights the importance of fusing various features at multiple positions along the structure to improve the performance of damage prediction. Specifically, sensor data from the ground, the top of the ground floor, and from different positions at the top of the structure provide valuable information for DS prediction in frame-type structures. When features characterizing the geometric configuration are added to the feature space, the number of floors significantly contributes to the predictions, showing the importance of this information to adapt the classifier to datasets with multiple floor-configurations. Finally, when MFs are available, the fundamental

frequency and the equivalent elastic modulus further improve the accuracy of damage prediction. This information facilitates the differentiation between model configurations that share the same amount of floors but vary in stiffness.

4. Application to real data of large-scale shake-table tests

The performance of the domain adaptation framework described in Section 2.7 is evaluated on the data from a large-scale masonry-infilled reinforced concrete (RC) frame. The specimen, tested by Stavridis et al. [90], was a two-dimensional three-floor frame structure and, therefore, complies with the modeled geometries considered in this study. However, the structural system differs, since the test structure consisted of RC frames and infill walls, while the numerical models used here represent unreinforced masonry shear-wall buildings. Therefore, the domain adaptation is performed for a challenging case of discrepancy between the simulated training set and the real building, on which damage classification is attempted.

4.1. Experimental data

The experimental structure (see Fig. 13a–b) represented existing buildings in California built in the 1920s. It was excited by the ground motion recorded during the 1989 Loma Prieta earthquake at the Gilroy Array #3 station, which was scaled to increasing amplitudes (see [90] for a more detailed description of the experimental campaign).

Damage classification is performed for eight tests, with intensities ranging from 20% to 120% of the original earthquake. Although many quantities and positions were monitored during the tests, the measured acceleration signals at five locations marked in Fig. 13b are used to compute the DSFs outlined in Section 2.4. The five sensors are chosen to comply with the simulated acceleration data that is used to train the classifier (see Fig. 2a).
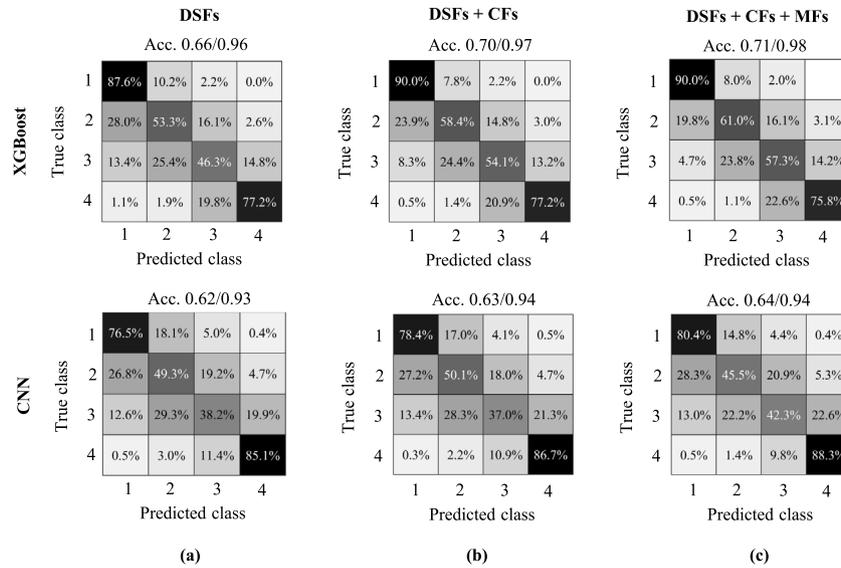
Fig. 11. Predictive performance of supervised ML approaches. Three sets of available features have been considered: (a) Only DSFs, (b) DSFs and CFs and (c) DSFs, CFs and MFs.
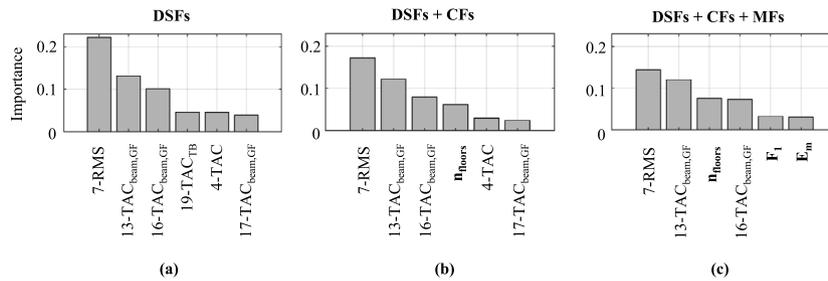

Fig. 12. Feature importance for the damage classification by the XGBoost architecture. Different feature-sets are considered: (a) Only DSFs, (b) DSFs and CFs and (c) DSFs, CFs and MFs.
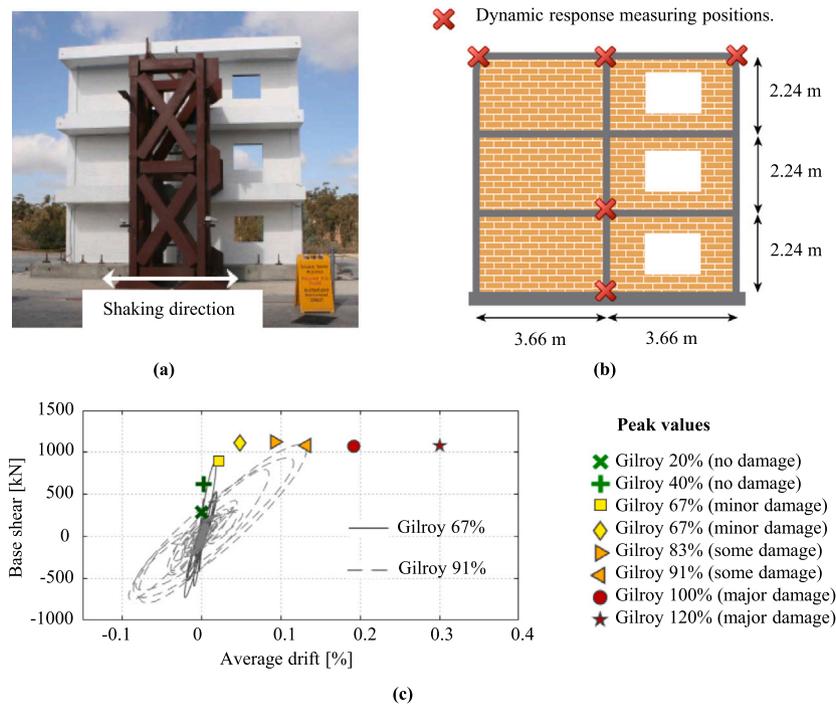

Fig. 13. Overview of the test specimen and dynamic tests: (a) photo of the tested specimen, (b) summary of sensor locations used to derive DSFs and dimensions of the specimen, (c) backbone curve of the peak displacements and corresponding base force, together with the response-history of two ground motions.
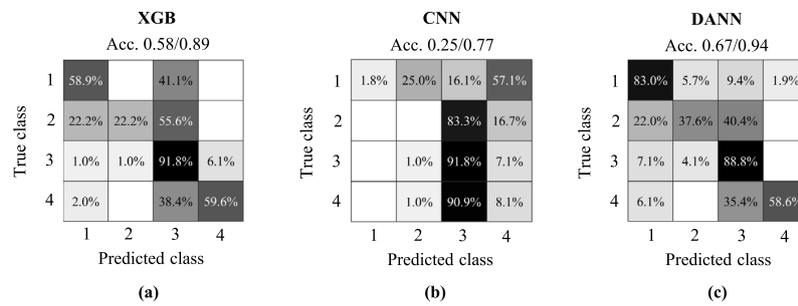
Fig. 14. Predictive performance of Machine learning algorithms in the target domain: (a) pre-trained XGBoost, (b) pre-trained CNN and (c) DANN.

The building capacity is approximated with the MRD and reaction force at the base that are reached during the earthquake tests, as shown in Fig. 13c. The backbone curve is comparable to the simulated pushover curves, which are used to define simulated DSs (see Fig. 4a). The DS observed in the specimen after each earthquake is also reported in Fig. 13c. Given that the characterization of the DS is based on observations and qualitative assessment, the DSs may not fully correspond to the definition used in the numerical simulations in this study. Yet, they reflect realistic conditions.

Following each earthquake motion, the structure was subjected to WN excitations with RMS amplitudes of 0.03 g and 0.04 g. These are used here to derive the DSFs. The application is based on real data and, thus, includes sensor noise and randomness of WN signals. However, it is noted that the amplitude of the WN excitation exceeds typical ambient vibrations and remains approximately constant over all test runs. Therefore, the monitoring data has a high signal-to-noise ratio.

4.2. Damage prediction with pre-trained classifiers

As a reference point, the predictive performance of the ML algorithms, pre-trained on simulation data (Section 3.2), is evaluated on the experimental data. The XGBoost and CNN classifiers are tested on DSFs derived from the WN excitation in different DSs. The test data is segmented into 10-second windows resulting in a total of 567 labeled datapoints with the following distribution:

- 261 DS 0 (46%)
- 109 DS 1 (19%)
- 98 DS 2 (17%)
- 99 DS 3 (17%)

Since the ML models are pre-trained exclusively with the simulation data, the entire set of experimental data can be used for testing. As explained in the following section, 50% of the healthy experimental data are used to train the domain adaptation network. To keep the same test set for the supervised and the DANN architectures, 50% of the healthy data, labeled DS 0, are excluded from the test set. Fig. 14a and b visualize the predictive performance of the pre-trained networks when exposed to the experimental data (target domain). The XGBoost architecture achieves an absolute accuracy of 58% and a soft accuracy of 89%. The confusion matrix exposes a significant bias towards predicted class 3 (DS 2), while the network shows poor performance in separating the healthy data (classes 1 and 2) from the damaged classes. CNN's performance is significantly worse, achieving an absolute accuracy of 25% and a soft accuracy of 77%. Again, there is a clear bias with respect to predicted class 3. These results expose the inability of pre-trained networks to generalize their predictive performance in domains that differ significantly from the training set. ML classifiers overfit to the source domain (simulations) and thus cannot adapt to the target domain, which differs from the source domain in terms of material (RC vs. simulated masonry), structural system (in-filled RC frame vs. unreinforced masonry walls), and origin (simulations vs. experimental data with inherent noise).

4.3. Damage prediction with domain adaptation

Domain adaptation aims to improve the predictive performance of a classifier in the target domain, for which only limited data are available, referring exclusively to the healthy state of the structure. The DANN architecture described in Section 2.7 is deployed, comprising three elements: a latent-space feature extractor, a damage classifier, and a domain discriminator. Apart from the common training set that contains the simulation data (Fig. 4c), 50% of the healthy data from the target domain (DS 0) are considered for training, without providing the label of their DS. The remaining experimental data is kept for testing. Finally, a binary domain label is attributed: 0 for the source domain and 1 for the target domain.

Fig. 14c illustrates the performance of the DANN network in the target domain. Absolute accuracy reaches 67% and the soft accuracy 94%, showing a significant improvement compared to the pre-trained networks. The DANN successfully separates the healthy class (DS 0) from the damaged classes. Furthermore, the heavy damage classes (DS 2 and 3) are successfully separated from the minor damage (DS 0 and 1). The prediction of DS 1 is only correct in 37.6% of the cases, although the confusion is limited to ±1 DSs. It is mentioned that the definition of damage in the experimental data was based on visual observations and involved qualitative evaluations of DS based on four empirical levels, namely "no damage", "minor damage", "some damage" and "major damage". Similar qualitative levels have been adopted for the formulation of damage thresholds in the simulation data, as described in Section 2.2. Although the hard assumptions for the DS thresholds do not directly affect the healthy state and the heavy damaged states, DS 1 and DS 2 are sensitive to the exact values of the thresholds and the assumptions made when deriving the equivalent yield point. Therefore, the observed uncertainty in predicting DS 1, as well as the partial confusion between DS 2 and 3 are deemed acceptable.

Overall, the deployed domain adaptation framework yields satisfactory results in predicting DS in the target domain, from which very limited and unlabeled data is considered, referring exclusively to the reference (healthy) state. In a practical context, this data can be acquired through ambient vibration measurements prior to an earthquake. By comparing the performance of the DANN with the corresponding pre-trained CNN, sharing the same architecture in the feature extractor and the damage classifier segments, a significant improvement in prediction accuracy is achieved. The limited information from the experiments, which does not contain data from damaged configurations, allows the DANN network to adapt successfully to the target domain. These results demonstrate the potential of DANN to transfer knowledge from numerical simulations to real-world monitoring applications.

5. Conclusions

This paper contains a thorough comparison of the damage classification performance of a large ensemble of DSFs, evaluated on an extensive dataset of nonlinear simulations of masonry structures with

varying geometrical configurations and material properties. With two popular machine learning classifiers, namely the XGBoost and CNN, multiple features have been fused into robust damage indicators. Finally, a DANN architecture is used to generalize the damage classification knowledge obtained from numerical simulations to real-world data from a large-scale shake-table test.

Fragility functions, involving individual DSFs, are used to compare their predictive performance with EDPs and IMs. DSFs, which are measurable, are shown to outperform PGA, which is a widely used IM to characterize the ground motion intensity, especially for regional risk and damage assessment. Although EDPs outperform individual DSFs in predicting damage, their monitoring in real applications is challenging, thus rendering their use impractical. However, fusing information of multiple features through ML algorithms significantly increases the accuracy of damage prediction, even beyond the accuracy achieved with individual EDPs. Therefore, ML-based fusion of vibration-based DSFs comprise a practical alternative for damage-tagging in the aftermath of earthquakes.

Attempting to generalize the knowledge obtained from simulations to real structures, a domain adaptation framework that capitalizes on DANNs is formulated and evaluated on large-scale shake-table data. Domain adaptation leverages limited data from a new domain (i.e., the real structure) to improve the predictive performance of a classifier that is trained in a known domain (i.e., numerical simulations). Comparing the performance of the DANN with pre-trained ML networks, a significant improvement in the accuracy of predicted DSs is observed. By exploiting very limited information from the experimental data, pertaining exclusively to the healthy state, the DANN network adapts successfully to the target domain, which differs from the source domain in terms of structural system (RC frames instead of unreinforced masonry shear walls) and data quality (simulations instead of experimental data with inherent noise). The successful domain adaptation in such an extreme case of divergence between the source and target domains demonstrates the powerful potential of DANN in transferring knowledge from simulations to real-world monitoring applications.

This paper proposes a framework that combines traditional SHM techniques with novel ML tools to fuse information from various measurable features into robust damage indicators. Additionally, by deploying a domain adaptation framework, it is demonstrated – in practical terms – how knowledge obtained from simulations can be harvested to improve damage detection and post-event safety tagging of real buildings, where labeled data are scarce.

Funding

Declaration of competing interest

The authors declare that they have no known competing financial interests or personal relationships that could have appeared to influence the work reported in this paper.

Data availability

Data will be made available on request.

References

[1] Galloway B, Hare J, Brunsdon D, Wood P, Lizundia B, Stannard M. Lessons from the post-earthquake evaluation of damaged buildings in Christchurch. Earthq Spectra 2014;30(1):451–74.

[2] Lin S-L, Uma S, King A. Empirical fragility curves for non-residential buildings from the 2010–2011 canterbury earthquake sequence. J Earthq Eng 2018;22(5):749–77.

[3] Lagomarsino S, Giovinazzi S. Macroseismic and mechanical models for the vulnerability and damage assessment of current buildings. Bull Earthq Eng 2006;4(4):415–43.

[4] Kircher CA, Whitman RV, Holmes WT. HAZUS earthquake loss estimation methods. Nat Hazards Rev 2006;7(2):45–59.

[5] Iervolino I, Chioccarelli E, Suzuki A. Seismic damage accumulation in multiple mainshock–aftershock sequences. Earthq Eng Struct Dyn 2020;49(10):1007–27.

[6] Marquis F, Kim JJ, Elwood KJ, Chang SE. Understanding post-earthquake decisions on multi-storey concrete buildings in Christchurch, New Zealand. Bull Earthq Eng 2017;15(2):731–58.

[7] Salawu O. Detection of structural damage through changes in frequency: A review. Eng Struct 1997;19(9):718–23.

[8] Carden EP, Fanning P. Vibration based condition monitoring: A review. Struct Health Monit 2004;3(4):355–77.

[9] Hearn G, Testa RB. Modal analysis for damage detection in structures. J Struct Eng 1991;117(10):3042–63.

[10] Basseville M, Mevel L, Goursat M. Statistical model-based damage detection and localization: Subspace-based residuals and damage-to-noise sensitivity ratios. J Sound Vib 2004;275(3–5):769–94.

[11] Vidal F, Navarro M, Aranda C, Enomoto T. Changes in dynamic characteristics of Lorca RC buildings from pre-and post-earthquake ambient vibration data. Bull Earthq Eng 2014;12(5):2095–110.

[12] Gentile C, Guidobaldi M, Saisi A. One-year dynamic monitoring of a historic tower: Damage detection under changing environment. Meccanica 2016;51(11):2873–89.

[13] Lorenzoni F, Caldon M, da Porto F, Modena C, Aoki T. Post-earthquake controls and damage detection through structural health monitoring: Applications in l'Aquila. J Civ Struct Health Monit 2018;8(2):217–36.

[14] Frizzarin M, Feng MQ, Franchetti P, Soyoz S, Modena C. Damage detection based on damping analysis of ambient vibration data. Struct Control Health Monit 2010;17:368–85.

[15] Skłodowska AM, Holden C, Guéguen P, Finnegan J, Sidwell G. Structural change detection applying long-term seismic interferometry by deconvolution method to a modern civil engineering structure (New Zealand). Bull Earthq Eng 2021;19(9):3551–69.

[16] Shokrani Y, Dertimanis VK, Chatzi EN, N. Savoia M. On the use of mode shape curvatures for damage localization under varying environmental conditions. Struct Control Health Monit 2018;25(4):e2132.

[17] Limongelli MP. The interpolation damage detection method for frames under seismic excitation. J Sound Vib 2011;330(22):5474–89.

[18] Pandey A, Biswas M, Samman M. Damage detection from changes in curvature mode shapes. J Sound Vib 1991;145(2):321–32.

[19] Giordano PF, Limongelli MP. Response-based time-invariant methods for damage localization on a concrete bridge. Struct Concr 2020;21(4):1254–71.

[20] Kaya Y, Kocakaplan S, Şafak E. System identification and model calibration of multi-story buildings through estimation of vibration time histories at non-instrumented floors. Bull Earthq Eng 2015;13(11):3301–23.

[21] Jaishi B, Ren W-X. Damage detection by finite element model updating using modal flexibility residual. J Sound Vib 2006;290(1–2):369–87.

[22] Kaya Y, Safak E. Structural health monitoring: real-time data analysis and damage detection. In: Seismic structural health monitoring. Springer; 2019, p. 171–97.

[23] Kita A, Cavalagli N, Venanzi I, Ubertini F. A new method for earthquake-induced damage identification in historic masonry towers combining OMA and IDA. Bull Earthq Eng 2021;19(12):5307–37.

[24] Akhlaghi MM, Bose S, Mohammadi ME, Moaveni B, Stavridis A, Wood RL. Post-earthquake damage identification of an RC school building in Nepal using ambient vibration and point cloud data. Eng Struct 2021;227:111413. http://dx.doi.org/10.1016/j.engstruct.2020.111413.

[25] Rytter A. Vibrational based inspection of civil engineering structures. Dept. of Building Technology and Structural Engineering, Aalborg University; 1993.

[26] Atamturktur S, Li T, Ramage MH, Farajpour I. Load carrying capacity assessment of a scaled masonry dome: Simulations validated with non-destructive and destructive measurements. Constr Build Mater 2012;34:418–29.

[27] Reuland Y, Lestuzzi P, Smith IF. Measurement-based support for post-earthquake assessment of buildings. Struct Infrastruct Eng 2019;15(5):647–62.

[28] Kita A, Cavalagli N, Masciotta MG, Lourenço PB, Ubertini F. Rapid post-earthquake damage localization and quantification in masonry structures through multidimensional non-linear seismic IDA. Eng Struct 2020;219:110841.

[29] Avci O, Abdeljaber O, Kiranyaz S, Hussein M, Gabbouj M, Inman DJ. A review of vibration-based damage detection in civil structures: From traditional methods to machine learning and deep learning applications. Mech Syst Signal Process 2021;147:107077.

[30] Hoelzl C, Ancu L, Grossmann H, Ferrari D, Dertimanis V, Chatzi E. Classification of rail irregularities from axle box accelerations using random forests and convolutional neural networks. In: Data science in engineering, Volume 9. Springer; 2022, p. 91–7.

[31] Figueiredo E, Park G, Farrar CR, Worden K, Figueiras J. Machine learning algorithms for damage detection under operational and environmental variability. Struct Health Monit 2011;10(6):559–72.

[32] Dabetwar S, Ekwaro-Osire S, Dias JP. Damage Classification of Composites Using Machine Learning. In: Volume 13: Safety Engineering, Risk, and Reliability Analysis. American Society of Mechanical Engineers; 2019, http://dx.doi.org/10.1115/IMECE2019-11851.

[33] Tibaduiza D, Torres-Arredondo MÁ, Vitola J, Anaya M, Pozo F. A damage classification approach for structural health monitoring using machine learning. Complexity 2018;2018.

[34] Sun L, Shang Z, Xia Y, Bhowmick S, Nagarajaiah S. Review of bridge structural health monitoring aided by big data and artificial intelligence: From condition assessment to damage detection. J Struct Eng 2020;(5):04020073.

[35] Yuan X, Tanksley D, Li L, Zhang H, Chen G, Wunsch D. Faster post-earthquake damage assessment based on 1D convolutional neural networks. Appl Sci 2021;11(21):9844.

[36] Tsuchimoto K, Narazaki Y, Spencer BF. Development and validation of a post-earthquake safety assessment system for high-rise buildings using acceleration measurements. Mathematics 2021;9(15):1758.

[37] Sajedi SO, Liang X. A data-driven framework for near real-time and robust damage diagnosis of building structures. Struct Control Health Monit 2020;27(3):e2488.

[38] Mangalathu S, Sun H, Nweke CC, Yi Z, Burton HV. Classifying earthquake damage to buildings using machine learning. Earthq Spectra 2020;36(1):183–208.

[39] Sheibani M, Ou G. The development of Gaussian process regression for effective regional post-earthquake building damage inference. Comput-Aided Civ Infrastruct Eng 2021;36(3):264–88.

[40] Bodenmann L, Reuland Y, Stojadinovic B. Dynamic updating of building loss predictions using regional risk models and conventional post-earthquake data sources. In: Proceedings of the 31st European safety and reliability conference. Research Publishing Services; 2021, p. 1411–8.

[41] Gardner P, Liu X, Worden K. On the application of domain adaptation in structural health monitoring. Mech Syst Signal Process 2020;138:106550. http://dx.doi.org/10.1016/j.ymssp.2019.106550.

[42] Movsessian A, Cava DG, Tcherniak D. Interpretable machine learning in damage detection using Shapley additive explanations. ASCE ASME J Risk Uncertain Eng Syst A Mech Eng 2022;8(2):1–31. http://dx.doi.org/10.1115/1.4053304.

[43] Xu S, Noh HY. Knowledge transfer between buildings for post-earthquake damage diagnosis without historical data. In: Structural health monitoring 2019: Enabling intelligent life-cycle health management for Industry Internet of Things (IIOT) - Proceedings of the 12th international workshop on structural health monitoring, vol. 1, 2019, p. 404–11. http://dx.doi.org/10.12783/shm2019/32141.

[44] Pan SJ, Yang Q. A survey on transfer learning. IEEE Trans Knowl Data Eng 2010;22(10):1345–59. http://dx.doi.org/10.1109/TKDE.2009.191.

[45] Bull L, Gardner P, Dervilis N, Papatheou E, Haywood-Alexander M, Mills R, et al. On the transfer of damage detectors between structures: An experimental case study. J Sound Vib 2021;501:116072.

[46] Ganin Y, Lempitsky V. Unsupervised domain adaptation by backpropagation. 2014, http://dx.doi.org/10.48550/ARXIV.1409.7495.

[47] Wang Q, Michau G, Fink O. Domain adaptive transfer learning for fault diagnosis. 2019, http://dx.doi.org/10.48550/ARXIV.1905.06004.

[48] Ozdagli A, Koutsoukos X. Domain adaptation for structural fault detection under model uncertainty. Int J Progn Health Manag 2021;12(2). http://dx.doi.org/10.36001/ijphm.2021.v12i2.2948.

[49] Moehle J, Deierlein GG. A framework methodology for performance-based earthquake engineering. In: 13th world conference on earthquake engineering, 679, WCEE Vancouver; 2004.

[50] Krawinkler H, Miranda E. Performance-based earthquake engineering. In: Earthquake engineering: From engineering seismology to performance-based engineering, vol. 9, Boca Raton, FL: CRC press; 2004, p. 1–9.

[51] Yepes-Estrada C, Silva V, Rossetto T, D'Ayala D, Ioannou I, Meslem A, et al. The global earthquake model physical vulnerability database. Earthq Spectra 2016;32(4):2567–85.

[52] Silva V, Crowley H, Pinho R, Varum H. Extending displacement-based earthquake loss assessment (DBELA) for the computation of fragility curves. Eng Struct 2013;56:343–56.

[53] Sivori D, Cattari S, Lepidi M. A methodological framework to relate the earthquake-induced frequency reduction to structural damage in masonry buildings. Bull Earthq Eng 2022;1–36.

[54] Noh HY, Lignos DG, Nair KK, Kiremidjian AS. Development of fragility functions as a damage classification/prediction method for steel moment-resisting frames using a wavelet-based damage sensitive feature. Earthq Eng Struct Dyn 2012;41(4):681–96.

[55] Computers and Structures Inc (CSI). SAP2000 integrated software for structural analysis and design. Technical report, Berkeley, California, USA; 2020.

[56] Lagomarsino S, Penna A, Galasco A, Cattari S. TREMURI program: An equivalent frame model for the nonlinear seismic analysis of masonry buildings. Eng Struct 2013;56:1787–99. http://dx.doi.org/10.1016/j.engstruct.2013.08.002.

[57] Pasticier L, Amadio C, Fragiacomo M. Non-linear seismic analysis and vulnerability evaluation of a masonry building by means of the SAP2000 V.10 code. Earthq Eng Struct Dyn 2008;37(3):467–85. http://dx.doi.org/10.1002/eqe.770.

[58] Snoj J, Österreicher M, Dolšek M. The importance of ambient and forced vibration measurements for the results of seismic performance assessment of buildings obtained by using a simplified non-linear procedure: Case study of an old masonry building. Bull Earthq Eng 2013;11(6):2105–32. http://dx.doi.org/10.1007/s10518-013-9494-8.

[59] Ministero delle Infrastrutture e dei trasporti. NTC 2018: D.M. del ministero delle infrastrutture e dei trasporti del 17/01/2018. Aggiornamento delle norme tecniche per le costruzioni (in Italian). 2018, p. 198.

[60] OPCM. OPCM3274: Code for the seismic design, assessment and retrofitting of buildings. (in Italian), Italy: OPCM; 2003.

[61] CEN. EN 1998-3: 2005 Eurocode 8: Design of structures for earthquake resistance—Part 3: Assessment and retrofitting of buildings. Bruxelles: European Committee for Standardization; 2005.

[62] Lang K, Bachmann H. On the seismic vulnerability of existing buildings: A case study of the city of basel. Earthq Spectra 2004;20(1):43–66. http://dx.doi.org/10.1193/1.1648335.

[63] SIA. SIA 269/8 Erhaltung von tragwerken - Erdbeben. Maintenance of structures - Earthquakes, Zurich: Swiss Society of Engineers and Architects; 2017.

[64] CEN. EN 1996-1-1: Design of masonry structures. Bruxelles: European Committee for Standardization; 2013.

[65] Luzi L, Lanzano G, Felicetta C, D'Amico MC, Russo E, Sgobba S, et al. Engineering strong motion database (ESM) (Version 2.0). Istituto Nazionale di Geofisica e Vulcanologia (INGV); 2020, http://dx.doi.org/10.13127/ESM.2.

[66] Martakis P, Reuland Y, Imesch M, Chatzi E. Reducing uncertainty in seismic assessment of multiple masonry buildings based on monitored demolitions. Bull Earthq Eng 2022;20(9):4441–82. http://dx.doi.org/10.1007/s10518-022-01369-0.

[67] Fajfar P. Capacity spectrum method based on inelastic demand spectra. Earthq Eng Struct Dyn 1999;28(9):979–93.

[68] Akkar S, Sucuoğlu H, Yakut A. Displacement-based fragility functions for low-and mid-rise ordinary concrete buildings. Earthq Spectra 2005;21(4):901–27.

[69] Villar-Vega M, Silva V, Crowley H, Yepes C, Tarque N, Acevedo AB, et al. Development of a fragility model for the residential building stock in South America. Earthq Spectra 2017;33(2):581–604.

[70] Lestuzzi P, Podestà S, Luchini C, Garofano A, Kazantzidou-Firtinidou D, Bozzano C, et al. Seismic vulnerability assessment at urban scale for two typical swiss cities using risk-UE methodology. Nat Hazards 2016;84(1):249–69.

[71] Zheng W, Dan D, Cheng W, Xia Y. Real-time dynamic displacement monitoring with double integration of acceleration based on recursive least squares method. Measurement 2019;141:460–71. http://dx.doi.org/10.1016/j.measurement.2019.04.053.

[72] Welch P. The use of fast Fourier transform for the estimation of power spectra: A method based on time averaging over short, modified periodograms. IEEE Trans Audio Electroacoust 1967;15(2):70–3.

[73] Zhang Y-M, Huang Z, Xia Y. An adaptive multi-taper spectral estimation for stationary processes. Mech Syst Signal Process 2023;183:109629.

[74] Zhou Y-L, Cao H, Liu Q, Wahab MA. Output-based structural damage detection by using correlation analysis together with transmissibility. Materials 2017;10(8). http://dx.doi.org/10.3390/ma10080866.

[75] Zhou Y-L, Figueiredo E, Maia N, Perera R. Damage detection and quantification using transmissibility coherence analysis. Shock Vib 2015;2015.

[76] Porter K, Kennedy R, Bachman R. Creating fragility functions for performance-based earthquake engineering. Earthq Spectra 2007;23(2):471–89.

[77] Baker JW. Efficient analytical fragility function fitting using dynamic structural analysis. Earthq Spectra 2015;31(1):579–99.

[78] Iervolino I. Estimation uncertainty for some common seismic fragility curve fitting methods. Soil Dyn Earthq Eng 2022;152:107068.

[79] Orlacchio M, Baltzopoulos G, Iervolino I. State-dependent seismic fragility via pushover analysis. In: Proceedings of the 17th world conference on earthquake engineering, vol. 20, Sendai, Japan; 2020.

[80] Crowley H, Silva V, Kalakonas P, Martins L, Weatherill G, Pitilakis K, et al. Verification of the European seismic risk model (ESRM20). In: Proceedings of the 17th world conference on earthquake engineering, vol. 27, Sendai, Japan; 2020.

[81] Sousa L, Silva V, Marques M, Crowley H. On the treatment of uncertainties in the development of fragility functions for earthquake loss estimation of building portfolios. Earthq Eng Struct Dyn 2016;45(12):1955–76.

[82] Friedman JH. Greedy function approximation: A gradient boosting machine. Ann Statist 2001;29(5):1189–232. http://dx.doi.org/10.1214/aos/1013203451.

[83] Chen T, Guestrin C. XGBoost: A scalable tree boosting system. In: Proceedings of the 22nd ACM SIGKDD international conference on knowledge discovery and data mining. New York, NY, USA: ACM; 2016, p. 785–94. http://dx.doi.org/10.1145/2939672.2939785.

[84] Won J, Park J-W, Jang S, Jin K, Kim Y. Automated structural damage identification using data normalization and 1-dimensional convolutional neural network. Appl Sci 2021;11(6). http://dx.doi.org/10.3390/app11062610.

[85] Quqa S, Martakis P, Movsessian A, Pai S, Reuland Y, Chatzi E. Two-step approach for fatigue crack detection in steel bridges using convolutional neural networks. J Civ Struct Health Monit 2022;12(1):127–40. http://dx.doi.org/10.1007/s13349-021-00537-1.

[86] Zhang Y-M, Wang H, Mao J-X, Xu Z-D, Zhang Y-F. Probabilistic framework with Bayesian optimization for predicting typhoon-induced dynamic responses of a long-span bridge. J Struct Eng 2021;147(1):04020297. http://dx.doi.org/10.1061/(ASCE)ST.1943-541X.0002881.

[87] Swersky K, Snoek J, Adams RP. Freeze-thaw Bayesian optimization. 2014, http://dx.doi.org/10.48550/ARXIV.1406.3896, URL: https://arxiv.org/abs/1406.3896.

[88] Goodfellow IJ, Pouget-Abadie J, Mirza M, Xu B, Warde-Farley D, Ozair S, et al. Generative adversarial networks. 2014, http://dx.doi.org/10.48550/ARXIV.1406.2661.

[89] Martins L, Silva V. Development of a fragility and vulnerability model for global seismic risk analyses. Bull Earthq Eng 2021;19(15):6719–45.

[90] Stavridis A, Koutromanos I, Shing PB. Shake-table tests of a three-story reinforced concrete frame with masonry infill walls. Earthq Eng Struct Dyn 2012;41(6):1089–108.